IOP Conf. Series: Materials Science and Engineering **444** (2018) 082009 doi:10.1088/1757-899X/444/8/082009

CFD prediction of combustion in a swirl combustor

F Popescu[1], R A Mahu[1], N A Antonescu[2] and I V Ion[1]

[1]Thermal Systems and Environmental Engineering Department, "Dunarea de Jos" University of Galati, Galati, Romania
[2]Thermotechnics and Thermal Equipment Department, Technical University of Civil Engineering Bucharest, Romania

E-mail: florin.popescu@ugal.ro

Abstract. A numerical simulation has been performed to study the biogas combustion in a burner with premixed flame developed under a high intensity small-scale turbulent environment, corresponding to high Karlovitz conditions. The CFD simulations were validated against experimental data for burner running with methane (measured temperatures along the radiant tube and CO emission). The biogas combustion was compared with methane combustion and influence of excess air on combustion was observed. It has revealed that the combustion of biogas with excess air of 1.15 is similar to combustion of methane with same excess air, except the CO concentration which is lower for biogas. Increasing the excess air for biogas combustion leads to the change of flame front position, temperature distribution and higher CO concentration.

1. Introduction

It has been shown that burning of biogas in commercial burners is not feasible due to the impossibility of achieving combustion stability [1]. Combustion of low calorific value fuel gases (synthetic gas derived from coal or biomass, anaerobic digester gas, gases generated from steelworks: blast furnace gas and coke oven gas) is characterized, due to the high content of inert gas and composition variation by a very low combustion temperature, unstable flame and an incomplete burn-out when conventional combustion technologies are used and no other fuel is used as support fuel. The high levels of NO_x emissions are another problem. Several combustion technologies have been developed for low calorific fuels. The flameless technique has been investigated on different gaseous fuels like methane, ethane as well as biogas. Flameless combustion is also known as colourless distributed combustion, flameless oxidation, moderate or intense low oxygen dilution combustion or high-temperature air combustion (HiTac) [2]. Flameless combustion technology is appropriate for industrial systems like glass-making factories, cement industries, gas turbines, hot blast stoves, boilers and biogas flare systems. Gaswärme-Institute. V. Essen (GWI) developed a progressive combustion system based on the concept of flameless and continuous air staging (COSTAIR) [3]. The results have shown the potential of the burner to be used for several low calorific gas qualities. The combustion process is stable and achieved NO_x and CO emissions are lower than 20 ppm (3% O_2).

The main scope of this work is to develop a burner able to ensure a highly efficient, low-emissions and stable combustion of low calorific gaseous fuels. The very intensive mixing of fuel and combustion air and the prolonged contact between the unburnt mixture and the combustion products in the proposed combustion chamber design result in a stable flame without supporting fuels at a wide range of thermal loads. The premixed flame is developed under a high intensity small-scale turbulent

environment, corresponding to high Karlovitz conditions [4]. Due to the heat transfer process in the flame near the cold burner wall the flame stabilization is achieved. The low oxygen levels required for the complete combustion in case of high turbulent combustion processes along with reduced flame temperature lead to reduced NO_x generation.

To analyse the combustion characteristics of biogas, a three dimensional (3D) computational fluid dynamic (CFD) study has been performed. The developed CFD model was first validated against experimental data (measured temperatures along the radiant tube and measured CO emissions) for burner operation with methane. The biogas combustion is compared to the methane combustion and the effects of excess air on combustion characteristics are observed and discussed.

2. Numerical modelling

2.1. Geometry

A three-dimensional CAD model of the combustor was created, based on the following main dimensions: total diameter D=250 mm, total length L=500 mm, first and fourth chamber length l_1=l_4=100 mm, second and third camber length l_2=l_3=150 mm; all inter-combustion chamber diaphragms have d_i = 100 mm; the air inlet has a rectangular section of 70 x 70 mm, the fuel inlet has a circular section with d_f = 10 mm, and the mixture is tangentially forced into the first combustion chamber through a 70 x 15 mm reduced section. An overall wall thickness of 2 mm was considered. This was explicitly included in the model only for the diaphragms, all other wall thicknesses were accounted for implicitly in the numerical modelling phase. The combustor is made of nickel-chromium alloy.

Figure 1 presents a cut-away view of the geometrical model. The 250 mm outlet section of the model – a cylindrical body generated by sweeping the 4th chamber outlet section outwards, introduced for reducing the influence of the outlet boundary condition on the interior of the combustion chamber – is missing in this representation, but it can be observed in the mesh plots. One can notice that certain edges have been rounded (r=5 mm), specifically at the inlet pipe - combustion chamber wall intersection. This feature is meant to alleviate the typical issues encountered during the meshing process of such geometries and has no influence on the final results.

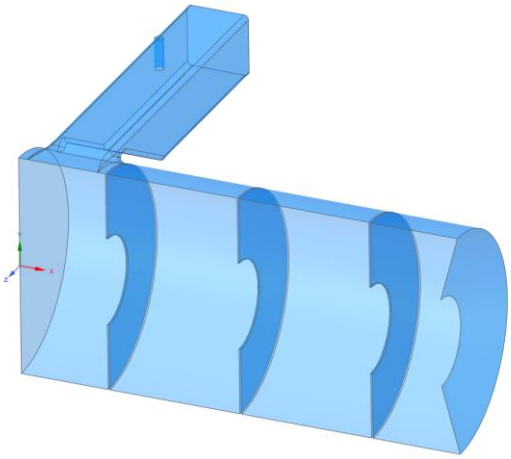

Figure 1. Cut-away view of the combustor CAD model.

2.2. Discretization mesh

Given the strongly non-linear character of the numerical problem to be solved, and the intended application of a scale-resolving turbulence modelling approach, the global quality of the mesh was considered to be of absolute importance. Therefore, no effort was spared during the design and creation of the mesh. The primary goal was to ensure high mesh size uniformity over the combustion

chamber volume, with adequate local density in the regions of interest (Figure 2). Taking advantage of the mostly cylindrical shape of the flow domain, which could be easily decomposed into simple volumes, a multi-block structured meshing approach was made possible in almost all regions, with few exceptions. The remaining zones were meshed using swept meshing algorithms, according to the locally dominant geometrical direction. Only the inlet pipe - combustion chamber wall intersection area had to be meshed with a combination of prismatic & tetrahedral cells. The maximum resulting edge length in the circumferential direction is 3.2 mm, while the maximum edge length parallel to the chamber axis is 2 mm. Due to the O-grid decomposition in the core region of the combustion chamber, the local resulting cell size is nearly uniform and around 1 mm. The near-wall mesh resolution was fixed at 0.5 mm, with a maximum growth ratio of 1.2. The secondary goal was to tightly control the cell skewness. The orthogonal shape of the grid blocks and the careful decomposition of the unstructured regions implicitly ensured a very high mesh quality (see Table 1).

Table 1. Mesh characteristics.

Mesh Statistics			Mesh Quality		
Nodes	Faces	Cells	Min. Skew	Max. Skew	Avg. Skew
6170654	19494907	6681064	0.0	0.6692	0.0557

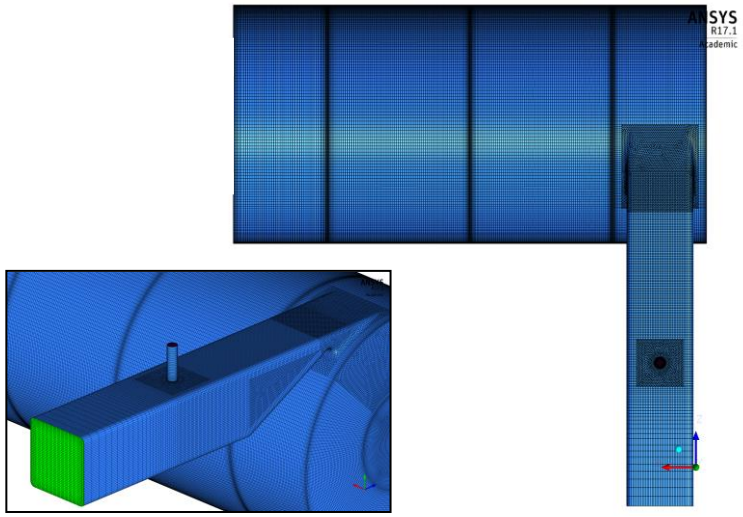

Figure 2. The spatial discretization mesh.

2.3. Physical modelling

2.3.1. Flow & turbulence

The high global physical instability of the rotational flow inside the combustion chamber, with very large pressure, density, velocity and temperature gradients across the entire flow field, consistently induced corresponding numerical instabilities and impeded any attempt to obtain a properly converged steady-state numerical solution. This effect was amplified by the low-dissipation spatial discretization schemes necessary for the scale-resolving (SR) flow modelling approach. Consequently, a steady-state RANS (*Reynolds-Averaged Navier-Stokes*) flow model was used only as a fast and robust numerical solution initialization step. The actual numerical solutions were determined based on a full unsteady N-S model coupled with the SAS (*Scale-Adaptive Simulation*) SST (*Shear-Stress Transport*) k-omega turbulence model [1]. The SAS concept [2] is based on the introduction of the von Kármán length-scale into the turbulence scale equation. The information provided by the von Kármán length-scale allows the SAS model to dynamically adjust to resolved structures in a URANS simulation, which results in an LES-like behaviour in unsteady regions of the flow field. At the same time, the model provides standard RANS capabilities in stable flow regions. It must be noted this flow instability

sensitivity is, by model definition, linked to the local mesh resolution and the time-step size, i.e. if the mesh is not fine enough and/or the local Courant number is too high, the predicted flow field will automatically revert to steady-state behaviour. Consequently, a much finer mesh than typically used for steady RANS simulations is necessary, but well below the requirements of a true Large-Eddy Simulation. The greatest advantage of SAS is, however, the physically consistent mathematical formulation of the unsteady term, which shields the model against improper application, allowing the user to better adapt the numerical simulation parameters (within certain limits) to the available hardware and time resources.

2.3.2. Species transport & reaction

The particular simulated combustion chamber can be considered a partially-premixed system due to the limited mixing of the fuel and air streams at the entrance of the first chamber. From a numerical point-of-view, a turbulent non-premixed type combustion system can be ideally simplified to a mixing problem ("mixed-is-burnt"), which translates into a greatly reduced computational effort as well; however, the partially or fully premixed systems are significantly more difficult to simulate due to the presence of a flame front, for which the propagation speed and position must also be predicted. For a given temperature and pressure, the laminar flame speed depends mainly on the local mixture composition, but the problem is more complicated than that for turbulent flows, because the local turbulence of the flow field plays a determinant role, and the effective flame speed can be significantly enhanced. Moreover, if turbulence is too high, the flame can be quenched, which adds to the complexity of the numerical problem. A first assumption was made that the finite-rate chemical kinetic effects are not important, which is a good approximation if slow chemical species evolution, like nitrogen oxides, are ignored. Furthermore, if the chemical scales of the reacting species are of the same order of magnitude, and the reaction itself is mainly limited to the flame front, the problem can be quite well approximated by tracking only the flame front propagation. One of the available models specifically designed for such approach is the C-Equation model, which solves a transport equation for the density-weighted mean reaction progress variable, denoted by $\bar{c}$:

$$\frac{\partial}{\partial t}\left(\rho\bar{c}\right)+\nabla\times\left(\rho\vec{v}\bar{c}\right)=\nabla\times\left(\left(\frac{k}{C_p}+\frac{\mu_t}{Sc_t}\right)\nabla\bar{c}\right)+\rho S_c \tag{1}$$

The progress variable is defined as a normalized sum of the product species mass fractions:

$$c=\frac{\sum_k\alpha_k\left(Y_k-Y_k^u\right)}{\sum_k\alpha_k\left(Y_k^{eq}-Y_k^u\right)}=\frac{Y_c}{Y_k^{eq}} \tag{2}$$

where superscript *u* and *eq* denote the unburnt reactant and chemical equilibrium, respectively. Based on this definition, unburnt mixture means c=0, whereas burnt mixture means c=1. The mean reaction rate in equation (1) is modelled as:

$$\rho S_c=\rho_u U_t\left|\nabla c\right| \tag{3}$$

where U_t is the turbulent flame speed (TFS). The model used in all the calculations for estimating TFS was the Zimont TFS closure model [3]. The flame stretch effect has also been included [4], which multiplies the source term for the progress variable with a stretch factor G representing the probability that the stretching will not quench the flame. The critical flame strain rate was set to 3000 1/s, at the lower bound for the typical range of near-stoichiometric methane flames [5].

Having taken care of the flame front position tracking problem, the remaining issue is the chemistry itself. One of the most elegant modelling approaches, from the engineering point-of-view, available for the simulation of flame front chemistry is the FGM (*Flamelet-Generated Manifold*) model [6]. The FGM model assumes that the thermo-chemical states in a turbulent flame are similar to the states in a laminar flame, and parameterizes these by mixture fraction and reaction progress.

Within the laminar flame, reaction progress variable (*c*) increases from 0 in the unburnt reactants to 1 in the burnt products, over a non-zero flame thickness. A point within the turbulent flame brush with $0 < c < 1$ has contributions from both fluctuating flame fronts, as well as the intermediate reaction progress. The FGM can be modelled with either premixed or diffusion laminar flamelets; both variants were tested, but only the results corresponding to the diffusion laminar flamelets approach are presented herein. A very important property of the FGM model is the theoretical capability to model not only the stirred reaction limit, but also the extreme flame states: ignition and extinction.

The flamelets were generated using the flamelet generator included in the simulation platform, starting from a reduced version of the GRI-MECH 1.2 reaction mechanism [7] that contains 19 species (+ N_2) and 84 reactions. The GRI mechanism is primarily intended for the simulation of natural gas combustion in air and, for example, is able to predict with reasonable accuracy the concentration and evolution of carbon monoxide. The PDF (probability density function) integrations were also taken care of outside the main computation, using the dedicated pre-processor. The generated files – reaction mechanism, flamelets file, and PDF file – were written to disk and reused for all computations. This method is valid as long as the chemical composition of the fuel remains within the limits of the original reaction mechanism derivation assumptions. Even with such a relatively complex reaction mechanism, the FGM combustion model is very low-demanding in terms of computational resources, especially compared to a Finite-Rate/Eddy-Dissipation-Concept approach, because it replaces direct chemical reaction integrations (very costly) with multi-dimensional table look-up operations.

To summarize, the FGM method is essentially a reduced-order modelling (ROM) technique, potentially very accurate, provided that the basis of reduction, i.e. the reaction mechanism and the flamelet calculation assumptions are valid, and computationally much cheaper than the full-scale physical system from which it originates.

2.3.3. Heat transfer

In order to obtain results comparable to the available experimental data, heat transfer inside the combustion chamber and at the computational domain boundaries had to model accordingly. The conductive and convective heat transfer is automatically handled by the solver, in both fluid and solid zones (internal diaphragms). Because the external walls of the combustion chamber were not explicitly included in the geometrical model, and consequently not present in the mesh either, the conductive heat transfer in the external walls volume was implicitly taken care of using the Shell-Conduction Model (SCM). The model automatically constructs a number of *n* layers with a given thickness and material properties, as specified by the user, by extruding the external wall faces outwards. This way, the effect of in-plane conduction, heat accumulation and thermal inertia of the chamber walls is accounted for. The external heat losses are also considered, in the form of both convection and radiation, with a reference temperature $T_{ref} = 300$ K. The convective heat transfer coefficient (HTC) for all external surfaces was estimated based on the assumption that only natural convection is taking place. The total emissivity values assigned to solid surfaces (0.75) is typical for cold-rolled steel sheets. The radiative heat exchange between internal surfaces was modelled by employing the DO (Discrete-Ordinates) grey radiation model. Although it is quite an expensive model, especially at higher discretization (for all cases, a 3 x 3 discretization per quadrant, with a 3 x 3 pixilation was assigned, which translates into 36 principal directions and just as many transport equations to solve!) it is the only reasonable solution for the investigated cases. This is due to the small optical thickness of the combustion chamber, which invalidates the use of simpler and less intensive radiation models, like Rosseland or P-1; on the other hand, the presence of radiation absorbing gases, like CO_2 and H_2O in the gaseous mixture, most notably for the biogas combustion cases, means that the significantly more economical, but similarly accurate S2S (Surface-to-Surface) radiation model is not applicable. The absorption coefficient, which is a function of local gas composition, was computed using the Weighted Sum of Grey Gases Model (WSGGM) with a domain-based length scale.

2.3.4. Physical modelling summary

Tables 2 and 3 presents a summary of all material properties and physical models used for the numerical simulations.

Table 2. Material Properties.

Property	Units	Mixture	Species
Density	kg/m^3	PDF	-
Specific Heat	J/kg/K	Mixing-law	Polynomial
Thermal Conductivity	W/m/K	Polynomial	-
Viscosity	Pa·s	Polynomial	-
Radiation Absorption Coeff.	-	WSGGM	-
Radiation Scattering Coeff.	-	0	-
Adiabatic Unburnt Mixture Density	kg/m^3	Pre-PDF Polynomial	-
Adiabatic Unburnt Mixture Temperature	K	Pre-PDF Polynomial	-
Unburnt Mixture Specific Heat	J/kg/K	Pre-PDF Polynomial	-
Unburnt Mixture Thermal Diff.	m^2/s	Pre-PDF Polynomial	-
Laminar Flame Speed	m/s	Pre-PDF Polynomial	-
Critical Flame Strain Rate	1/s	3000	-

Table 3. Physical Models.

Flow	Unsteady Reynolds-Averaged Navier-Stokes Model	
Turbulence	SAS SST k-omega Model	
Heat Transfer	Fluid Zones	Convective + Conductive Heat Transfer
	Solid Zones	Conductive Heat Transfer
	Solid Surfaces	Radiative Heat Transfer
		Shell Conduction Model (only external surfaces)
Combustion	Partially-Premixed Model	C-Equation Model
		Zimont Turbulent Flame Speed Model
		Flamelet-Generated Manifold Model

2.4. Numerical solver

Although the introduction of reduced-order modelling of chemical interactions through FGM virtually eliminates the characteristic stiffness associated with the solving of chemical species conservation equations, and implicitly reduces the non-linearity of the global system of equations, the very strong coupling between pressure, density and temperature of the burning mixture still exists.

For steady-state CFD simulations of such systems usually coupled implicit solvers are used. They feature very good stability and excellent convergence properties, especially the pressure-based variants. The main drawback of these solvers is their large memory footprint and high CPU requirements. For unsteady simulations, a low CPU and memory demanding numerical solver is generally advisable in order to reduce the overall computational effort, as a very high number time-steps and sub-iterations respectively, need to be performed, particularly for problems where statistically-steady solutions are to be obtained. Both a pressure-based implicit segregated solver and a pressure-based coupled implicit solver were employed during the testing phase of this study. For each type of solver, the optimal parameter setup for best stability and convergence has been separately determined. The observed behaviour during the trial simulations indicated that the coupled solver needs only little or no explicit under-relaxation of variables, reaches the same level of convergence per time-step in half as many sub-iterations or less, but it requires slightly more wall-clock time per time-step compared to the segregated approach. Far more importantly though, it also provides significantly better numerical stability, and for this reason it was preferred and consequently applied for all simulations. The spatial discretization schemes for each variable were chosen as presented in Table 4. With the exception of DO irradiation, all other variables discretization schemes are at least second order accurate in space. Given the importance of the momentum equation discretization, a bounded central differencing scheme was adopted for momentum, which has a significantly lower dissipation than a second-order upwind scheme. This increases the sensitivity of the numerical model to local

flow instabilities and enables the simulation to capture a much richer instantaneous velocity spectrum for a given time-step size. This, in turn, has a positive effect on the estimation of, for instance, the local turbulent flame velocity, and implicitly on the instantaneous position of the flame front. For the same reasons, a bounded second-order accurate backward Euler time integration scheme was selected.

Table 4. Discretization Schemes.

			Under-relaxation
Space	Pressure	Second-order Upwind	0.75
	Momentum	Bounded Central Differencing	0.75
	Density	Second-order Upwind	1
	Turbulence	Second-order Upwind	0.75
	Discrete Ordinates	First Order Upwind	1
	Energy	Second-order Upwind	1
	Species	Second-order Upwind	1
Time		Bounded Second-order Upwind	-

3. Numerical simulation

3.1. Boundary conditions

Due to the need to strictly control the total flow rates and composition of combustible mixture and the reaction conditions (mainly chamber pressure), the only available combination of boundary conditions (BC) that satisfy the requirements is "*mass-flow-inlet*" + "*pressure-outlet*". The inlets for methane/biogas and air have been separately represented in the numerical model (see Figure 3), which allows for a direct control of the flow ratio and inlet temperatures. All cases were setup with a static pressure at chamber outlet equal to the atmospheric pressure, and the temperature of both inlet fluxes equal to 300 K. The internal walls condition was implicitly setup as thermally coupled, and consequently all heat transfer parameters were automatically computed by the solver. The only parameter that was imposed was the total surface emissivity, specified as 0.8 for all solid surfaces. On the external walls a combined heat transfer through radiation and convection was defined. The reference background/exterior temperature for both radiative & convective heat exchange was taken as 300 K. The convective HTC was estimated to be around 5 W/m/K, which is typical for free convection in air. With this setup, quite strong and chaotic fluctuations of the calculated unsteady inlet static pressure have been observed, particularly at early stages of the simulations; as the mean values of flow variables were settled, the pressure fluctuations also manifested a tendency towards a steady average value, but were far from being removed, only dumped to a certain extent. This is probably a numerical effect of the boundary condition combination, which keeps the instantaneous mass flow rate fixed, forcing the unwanted oscillations in the pressure field. An attempt to replace the mass-flow-inlets with pressure-inlets was made, but with little success, and was therefore abandoned. The boundary conditions setup for the four cases included in this study is presented in Table 5.

Table 5. Boundary Conditions (Q_{CH4}=10Nm^3/h in all cases).

		Methane λ=1.15	Biogas λ=1.15	Biogas λ=1.20	Biogas λ=1.25
Inlet Air	Mass Flow [g/s]	36.00	36.00	37.57	39.13
	Temperature [K]	300	300	300	300
Inlet Fuel	Mass Flow [g/s]	1.822	5.931	5.931	5.931
	Temperature [K]	300	300	300	300
Outlet	Static Pressure [Pa]	0	0	0	0
Walls	Radiation, ε	0.8	0.8	0.8	0.8
	Convection, α [W/m/K]	5.0	5.0	5.0	5.0

3.2. Numerical simulation

All cases were initialized using the results of a steady-state calculation. This is not only useful for drastically reducing the amount of time needed to reach statistically steady flow conditions inside the combustion chamber, but also mandatory for the initialization of correct solid walls temperature. This is due to the fact that the unsteady simulations time scales are far too short to allow for the solid walls temperature to reach a statistically steady state (flow time scale is less than 0.1 s, solid time scale is well above 10 s, so a discrepancy of at least two orders of magnitude). To smooth out the transition between the steady and unsteady models, the SST k-omega model was used for turbulence in steady mode and switched to the SAS variant once the unsteady mode was activated.

Also for reducing the total computational effort, the time-step size was initially chosen larger than optimal for settling down the response of the transient model and more quickly reach the statistically steady regime. Once this regime was established, judged by monitoring several parameters of the model such as the burnt gases outlet temperature, or the concentration of certain chemical species, like CO, the time-step size was reduced such that the maximum instantaneous Courant number in the entire flow domain did not exceed a value of 10 (this ensured a volume-averaged Courant number of about 5 over the chamber core and less than 2 for the entire chamber – this is perfectly acceptable for the SAS model, as previously explained, but an order of magnitude higher than the requirements of LES) and the calculation was resumed. After reassessing the quasi-steady operational regime, the simulations were run for an additional 5,000 time-steps, during which period the solution was monitored and statistical data was gathered for all variables of interest, including pressure, velocity, temperature, heat fluxes, chemical species concentrations, reaction rates, etc. For example, the final time-step used for Case 1 calculation was 5.e-5 s, and the resulting total sampling time was 0.25 s, which is equivalent to approximately two times the average fluid residence time for the simulated conditions.

The calculations were run accessing between 192 and 384 cores per case within the existing 624 core HPC Cluster.

4. Computational results

The computational results obtained for two different fuels, methane and biogas, are included below (Figures 3-20). The composition of biogas was simplified to a mixture of 55% methane and 45% carbon dioxide, by volume. For all computational cases the volumetric flow rate of the methane fraction was identical and equal to 10 Nm^3/h. In the case of biogas, three air-fuel ratios have been tested, while for methane only one air-fuel ratio is presented. A table summarizing the main outputs of each case is available, containing the time & area-averaged values for: chemical species of interest and their concentration as mass fractions, mixture temperature and static pressure, as determined by numerical simulation at the two inlets and the four outlet openings of each individual section of the combustion chamber (Tables 6-9).

Table 6. Results for case 1 (Methane, Q_{CH4} = 10 Nm^3/h, λ = 1.15).

Section	CH_4	CO	CO_2	H_2	H_2O	O_2	T [K]	p_{st} [Pa]	MFR* [g/s]
Inlet_air	0.0	0.0	0.0	0.0	0.0	2.330E-01	300	2656	36.00
Inlet_fuel	1.0	0.0	0.0	0.0	0.0	0.0	300	2694	1.822
Chamber-1_out	2.136E-04	1.703E-02	1.279E-01	5.755E-04	1.203E-01	8.214E-03	2038.1	356.4	-
Chamber-2_out	3.691E-09	1.746E-02	1.284E-02	5.568E-04	1.208E-01	6.351E-03	1839.2	196.8	-
Chamber-3_out	7.923E-11	1.459E-02	1.320E-01	4.537E-04	1.213E-01	5.438E-03	1655.9	90.4	-
Chamber-4_out	4.289E-10	1.313E-02	1.332E-01	4.079E-04	1.209E-01	6.039E-03	1556.3	19.5	-

*MFR – mass flow rate

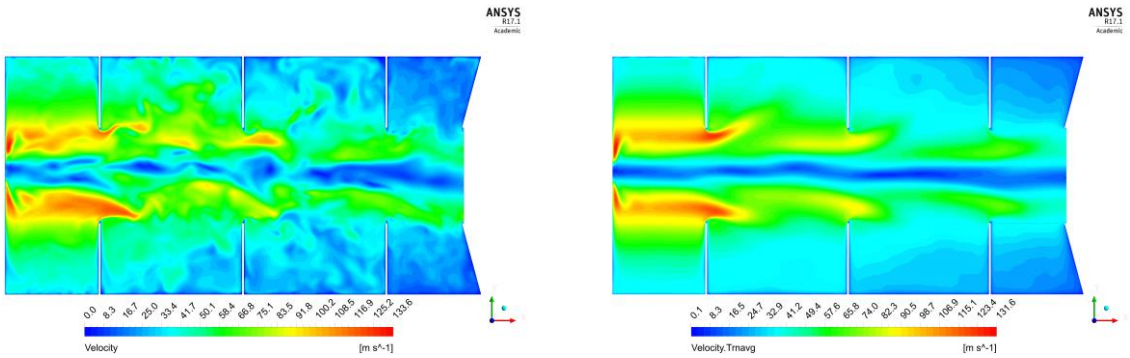

Figure 3. The instantaneous (left) and time-averaged (right) contours of velocity magnitude on an axial plane.

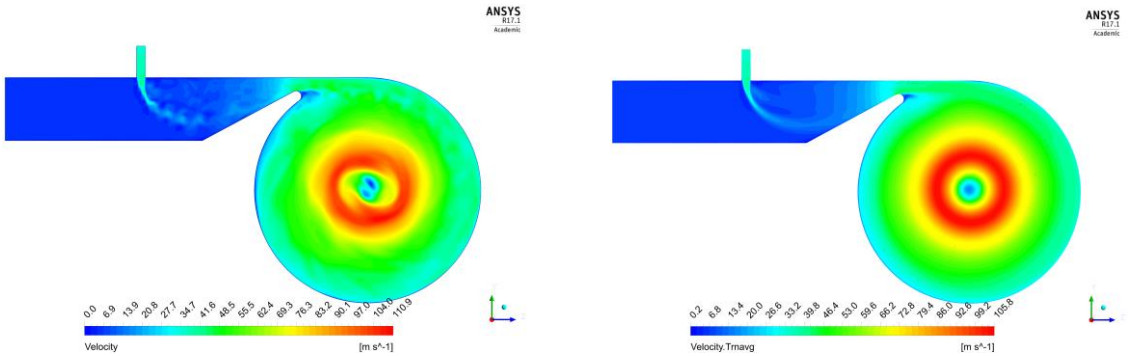

Figure 4. The instantaneous (left) and time-averaged (right) contours of velocity magnitude on a normal plane passing through the inlet pipe.

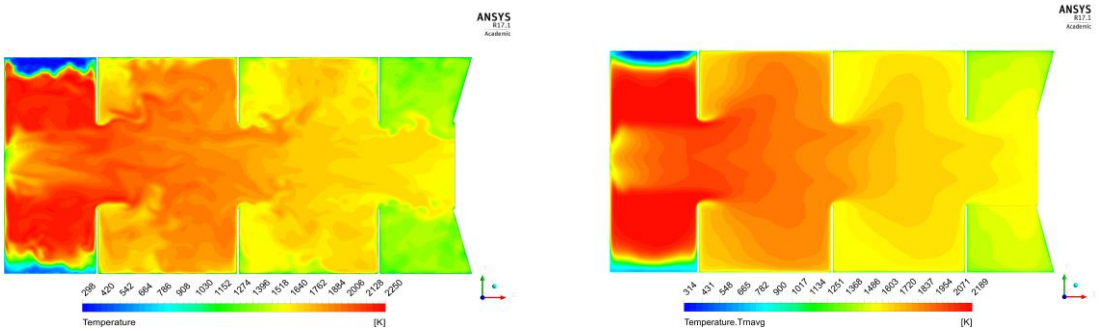

Figure 5. The instantaneous (left) and time-averaged (right) contours of temperature on an axial plane.

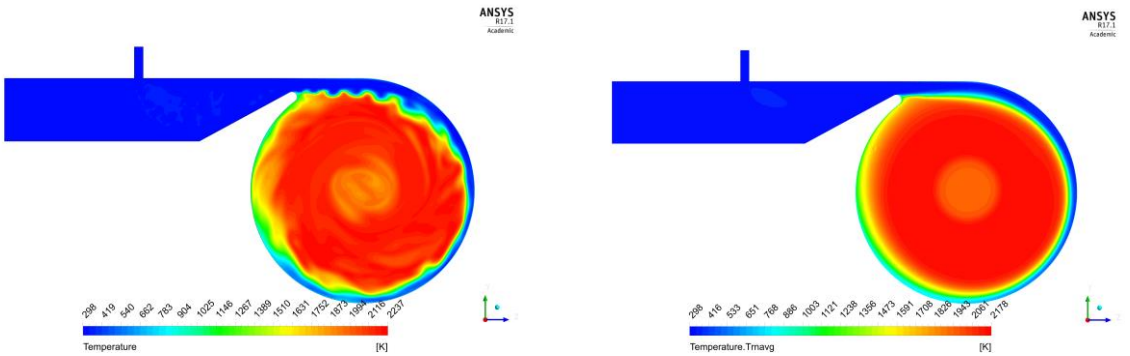

Figure 6. The instantaneous (left) and time-averaged (right) contours of temperature on a normal plane passing through the inlet pipe.

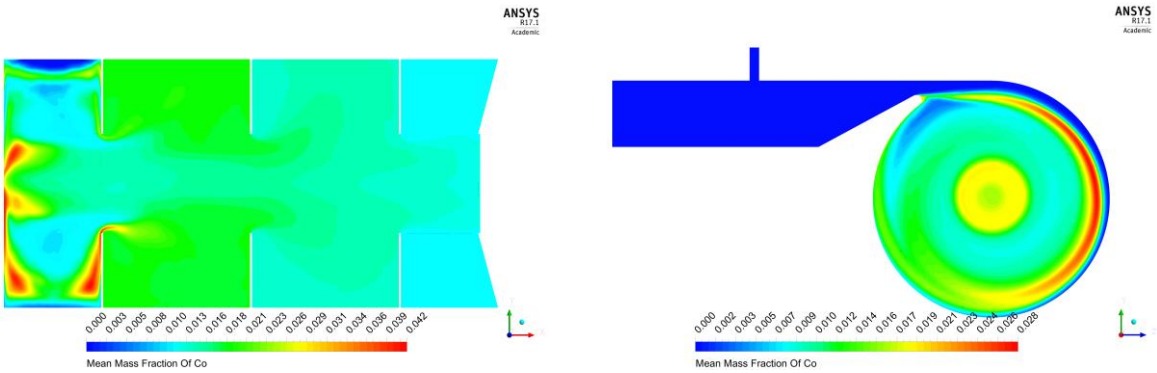

Figure 7. The time-averaged contours of CO mass fraction on an axial plane (left) and on a normal plane passing through the inlet pipe (right).

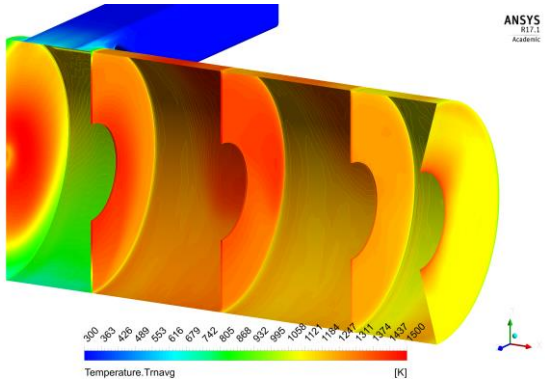

Figure 8. The time-averaged contours of temperature on solid walls.

Table 7. Results for case 2 (Biogas, Q_{CH4} = 10 Nm^3/h, λ = 1.15).

Section	CH_4	CO	CO_2	H_2	H_2O	O_2	T [K]	p_{st} [Pa]	MFR [g/s]
Inlet_air	0.0	0.0	0.0	0.0	0.0	2.330E-01	300	2789	36.00
Inlet_fuel	3.082E-01	0.0	6.918E-01	0.0	0.0	0.0	300	3025	5.931
Chamber-1_out	1.170E-04	1.217E-02	2.239E-01	2.278E-04	1.063E-01	1.005E-02	1886.8	306.6	-
Chamber-2_out	1.795E-10	1.092E-02	2.252E-01	1.940E-04	1.064E-01	9.376E-03	1701.1	164.7	-
Chamber-3_out	1.074E-10	9.797E-03	2.249E-01	1.735E-04	1.057E-01	1.056E-02	1520.4	79.1	-
Chamber-4_out	5.488E-10	8.967E-03	2.244E-01	1.585E-04	1.050E-01	1.169E-02	1427.0	21.7	-

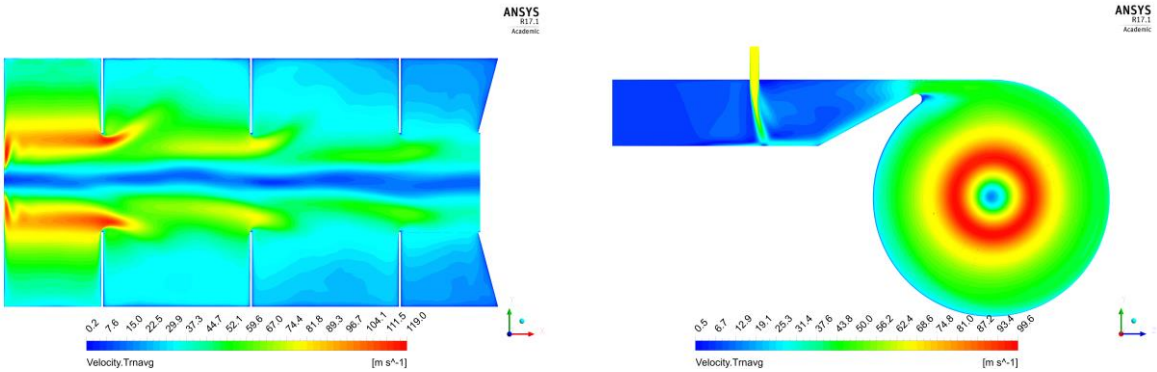

Figure 9. The time-averaged contours of velocity magnitude on an axial plane (left) and on a normal plane passing through the inlet pipe (right).

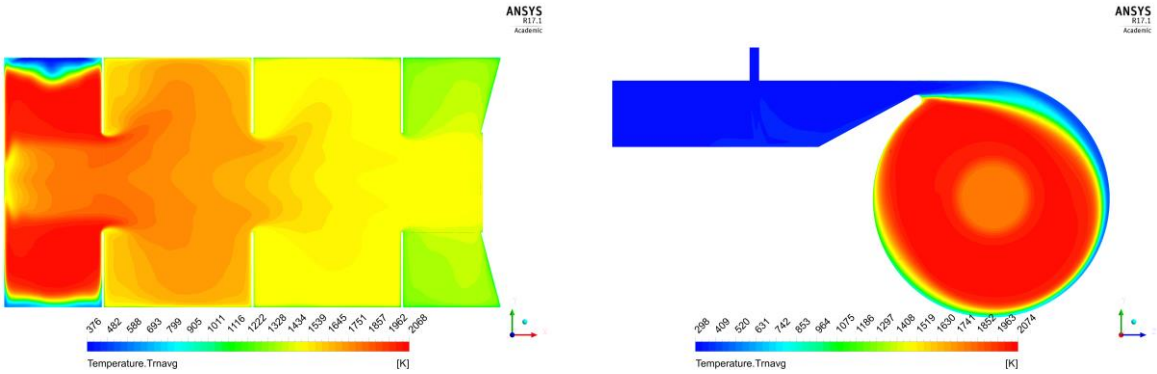

Figure 10. The time-averaged contours of temperature on an axial plane (left) and on a normal plane passing through the inlet pipe (right).

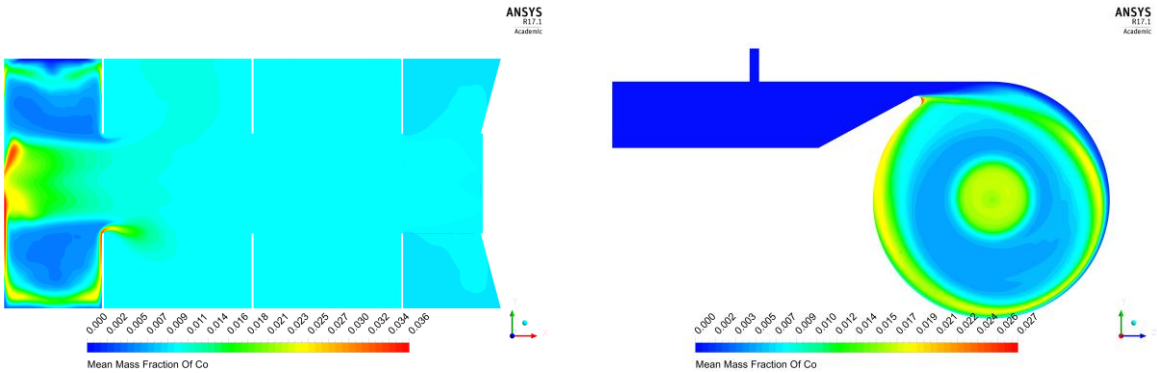

Figure 11. The time-averaged contours of CO mass fraction on an axial plane (left) and on a normal plane passing through the inlet pipe (right).

Table 8. Results for case 3 (Biogas, Q_{CH4} = 10 Nm^3/h, λ = 1.20).

Section	CH_4	CO	CO_2	H_2	H_2O	O_2	T [K]	p_{st} [Pa]	MFR [g/s]
Inlet_air	0.0	0.0	0.0	0.0	0.0	2.330E-01	300	6000	37.57
Inlet_fuel	3.082E-01	0.0	6.918E-01	0.0	0.0	0.0	300	6232	5.931
Chamber-1_out	1.388E-02	8.004E-03	1.839E-01	1.469E-04	7.251E-02	7.057E-02	1557.8	508.7	-
Chamber-2_out	1.139E-04	1.272E-02	2.133E-01	2.354E-04	1.014E-01	1.933E-02	1884.8	236.6	-
Chamber-3_out	1.116E-09	1.068E-02	2.154E-01	1.956E-04	1.014E-01	1.863E-02	1711.5	115.9	-
Chamber-4_out	6.414E-10	1.049E-02	2.148E-01	1.921E-04	1.011E-01	1.933E-02	1602.5	34.8	-

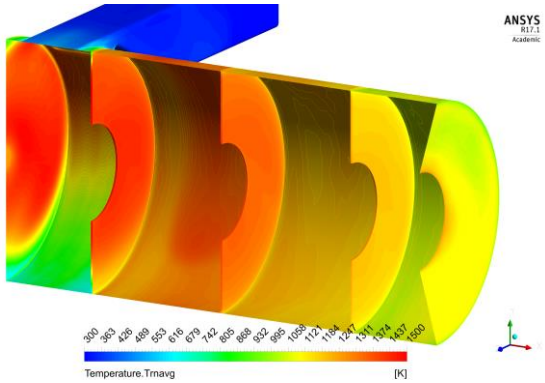

Figure 12. The time-averaged contours of temperature on solid walls.

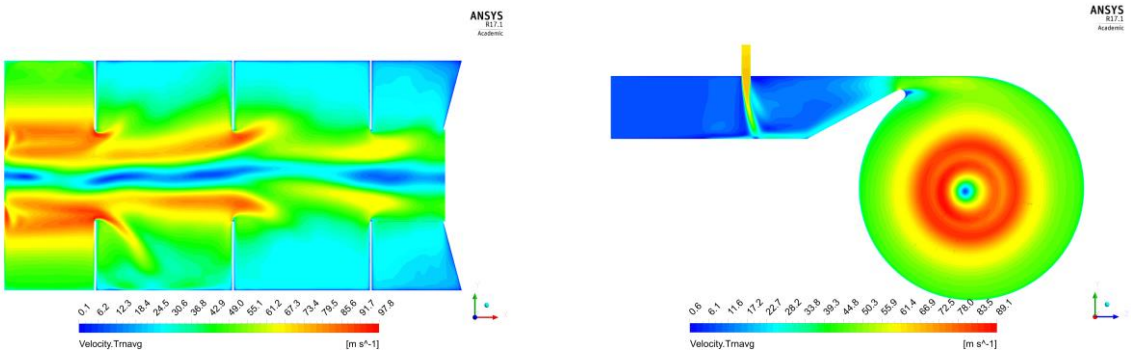

Figure 13. The time-averaged contours of velocity magnitude on an axial plane (left) and on a normal plane passing through the inlet pipe (right).

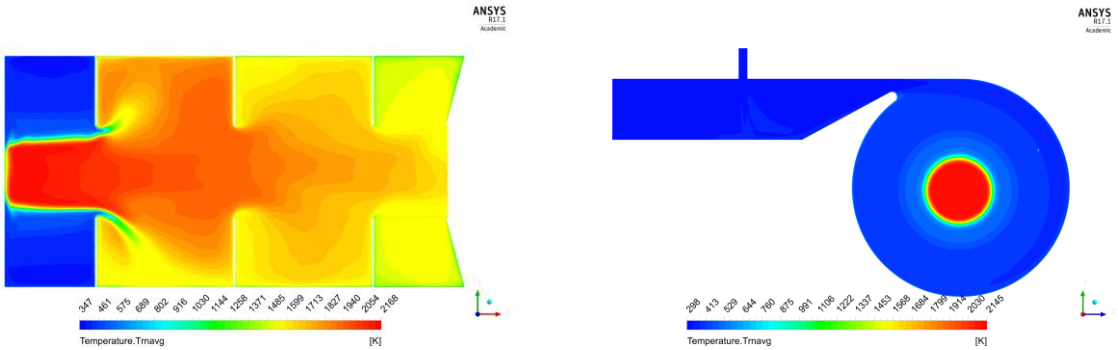

Figure 14. The time-averaged contours of temperature on an axial plane (left) and on a normal plane passing through the inlet pipe (right).

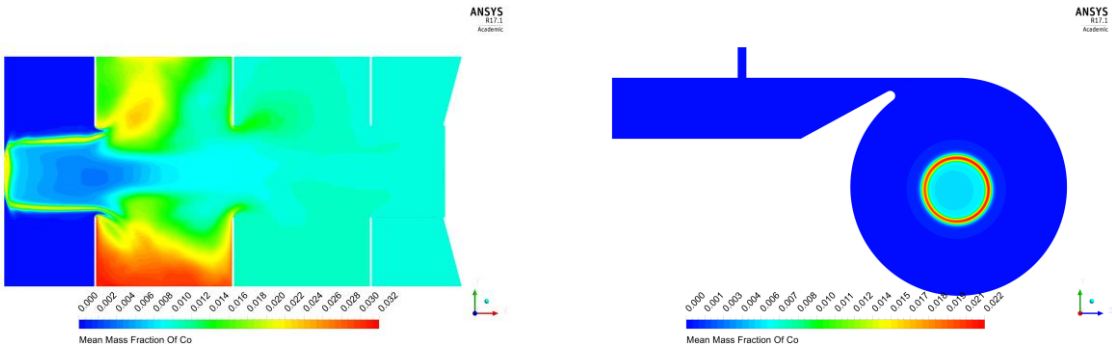

Figure 15. The time-averaged contours of CO mass fraction on an axial plane (left) and on a normal plane passing through the inlet pipe (right).

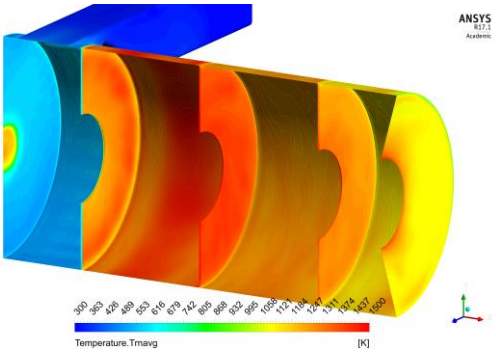

Figure 16. The time-averaged contours of temperature on solid walls.

Table 9. Results for case 4 (Biogas, Q_{CH4} = 10 Nm^3/h, λ = 1.25).

Section	CH_4	CO	CO_2	H_2	H_2O	O_2	T [K]	p_{st} [Pa]	MFR [g/s]
Inlet_air	0.0	0.0	0.0	0.0	0.0	2.330E-01	300	6621	39.13
Inlet_fuel	3.082E-01	0.0	6.918E-01	0.0	0.0	0.0	300	6851	5.931
Chamber-1_out	1.379E-02	6.667E-03	1.755E-01	1.182E-04	6.817E-02	7.941E-02	1511.1	543.7	-
Chamber-2_out	3.005E-04	1.210E-02	2.033E-01	2.169E-04	9.642E-02	2.944E-02	1833.6	252.5	-
Chamber-3_out	3.305E-09	8.256E-03	2.106E-01	1.508E-04	9.803E-02	2.503E-02	1681.0	122.3	-
Chamber-4_out	1.713E-08	8.183E-03	2.119E-01	1.492E-04	9.860E-02	2.389E-02	1574.2	39.0	-

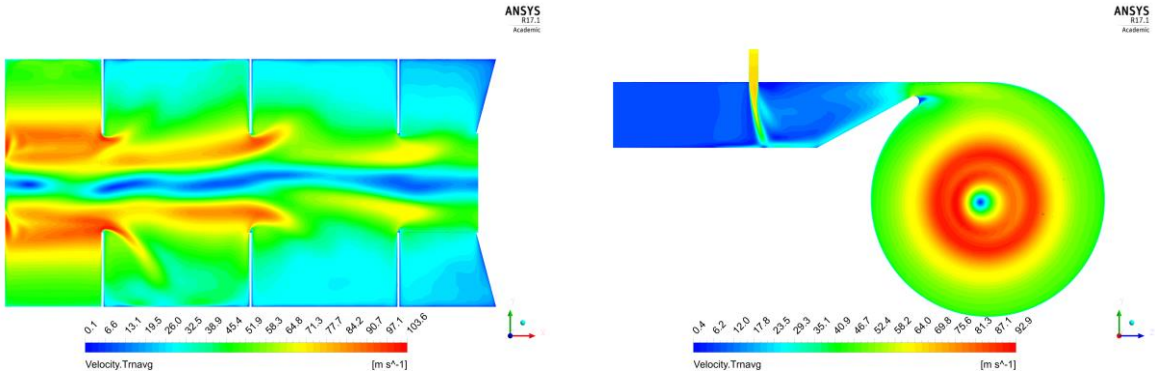

Figure 17. The time-averaged contours of velocity magnitude on an axial plane (left) and on a normal plane passing through the inlet pipe (right).

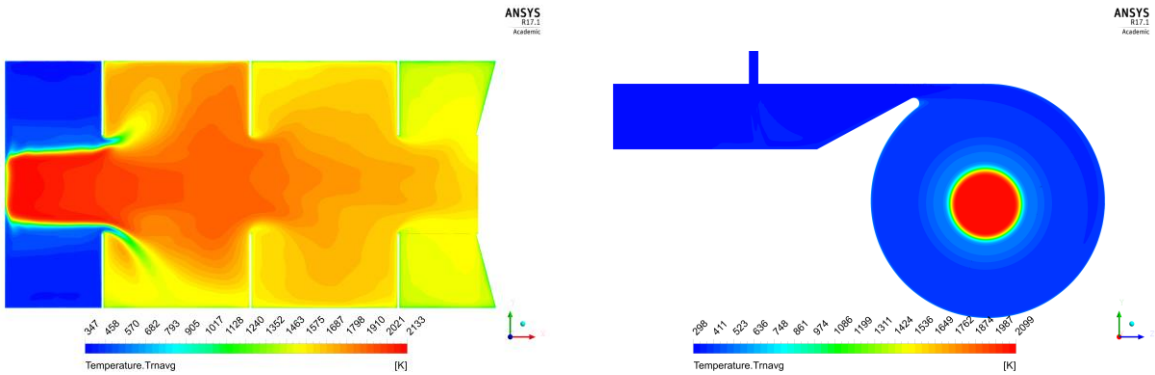

Figure 18. The time-averaged contours of temperature on an axial plane (left) and on a normal plane passing through the inlet pipe (right).

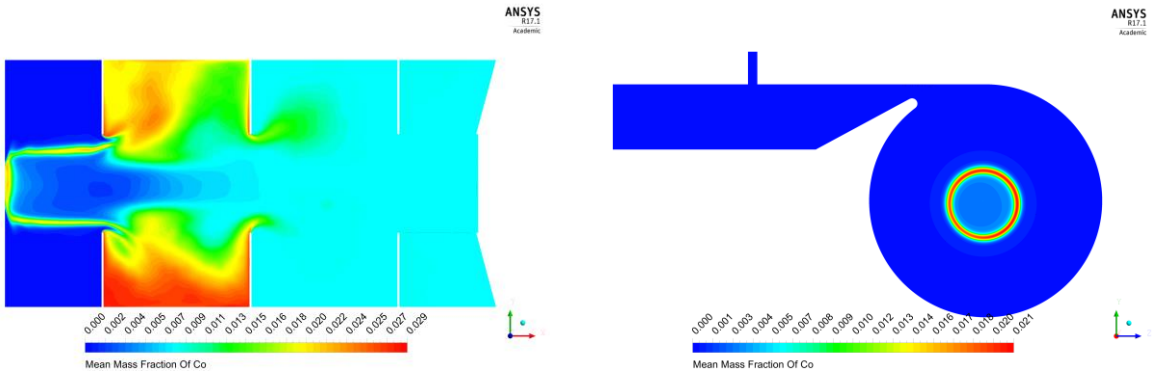

Figure 19. The time-averaged contours of CO mass fraction on an axial plane (left) and on a normal plane passing through the inlet pipe (right).

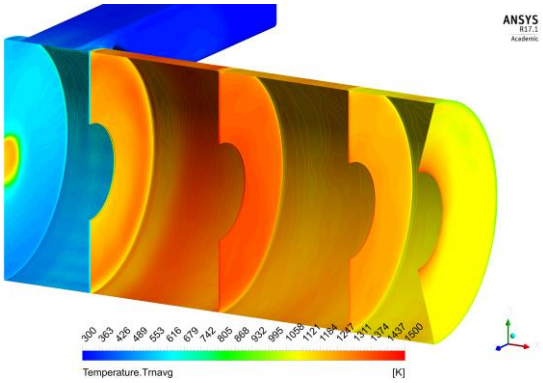

Figure 20. The time-averaged contours of temperature on solid walls.

5. Results analysis

The instantaneous plots are shown only for the first case, pure methane, for direct comparison with the corresponding time-averaged plots. The relatively large time-step size inevitably introduces a certain level of damping on the velocity field, and consequently on all fields, but even so, the resolution of the vertical structures is perfectly acceptable when correlated to the scale of the flow domain. By closely analysing the time-averaged plots it can be noticed that the mean variables did not reach full convergence yet, however we consider that the extra effort necessary to achieve that is simply unjustified, especially if considering that the gain in overall accuracy would be practically null.

A Rankine-type vortex, typical for cyclones - i.e. a forced vortex core, with a diameter roughly equal to the internal diaphragm diameter, surrounded by a free vortex extending radially towards the outer cylindrical wall of the combustion chamber – is clearly visible in the first section of the combustor. Due to the friction with the solid walls, the intensity of the vertical motion is gradually slowed down in the following sections, although not entirely; at the exit section of the combustion chamber the tangential component of the flow is still very important. The circumferential circulation is reduced in the third section and effectively limited to the core region in the fourth section.

The very low static pressure in the vortex core promotes a reversed flow around the combustion chamber axis over the entire chamber length. Most of the total pressure losses take place between the inlet boundaries and the exit of the first section of the combustion chamber, this being the effect of the high near-wall velocities, reaching more than 50 m/s at the reduced inlet section and over the entire circumference of the chamber.

The flame front is stabilized near the external cylindrical wall of the first section, without touching it; the unburnt mixture of fuel and air separates the flame front from the chamber wall. This reduces the actual thermal load of the cylindrical wall, maintaining the wall temperature around 900 K. Much higher temperatures are observed on the bottom wall and in the next sections, specifically on the separation diaphragms, locally exceeding 1500 K. The maximum average combustion temperature for pure methane is about 2190 K, and is almost uniform over the volume of the first section; however, the burnt gaseous mixture temperature drops quickly in the next sections down to about 1550 K at the chamber exit. This is caused by the intense radiative heat loss through the chamber external walls.

The two cases with air-excess ratio $\lambda = 1.15$, one with pure methane and the other with biogas as fuel, they are quite similar in almost all aspects (Figures 21-23), the most notable differences being the concentration and distribution of carbon monoxide. Significantly lower values of CO are generated for biogas combustion, which is mostly due to the presence of a large fraction of CO_2 in the unburnt mixture. A slightly higher pressure loss was calculated, implicitly caused by the higher volumetric flow and mixture velocities at the inlet of the first section of the combustor.

The higher air excess biogas cases (1.2 and 1.25 respectively) are however very different from the first two cases. The most notable modification is the shifting of the flame front position from the initial near-wall position at the exterior of the first section to the core vortex boundary. This strongly alters the velocity distribution in all sections, reducing the velocity drop from first section outlet towards the

exit of the combustion chamber. The maximum temperature is now located in the core, and the temperature gradient along the axis is lower. Evidently, the solid walls temperature is also significantly changed, with almost the entire surface of the first section external walls barely heated, the average temperature being less than 600 K. Only one spot at the back of the chamber is visibly hotter, above 1000 K. The maximum wall temperature is still located in the second section, but the second diaphragm wall is significantly more thermally loaded than the first wall. The outlet concentration of CO is higher at $\lambda = 1.2$ than at $\lambda = 1.15$, but lowers again with increasing air excess. Most of the CO is now concentrated in the second section of the combustor.

The most striking difference is the massively increased pressure loss. This is most certainly the effect of the flame front repositioning, although the actual mechanism of its action is not yet clear. The increase in volumetric flow cannot explain this all by itself, the pressure loss effectively doubles, but the flow only increases by approx. 4% and 8% respectively.

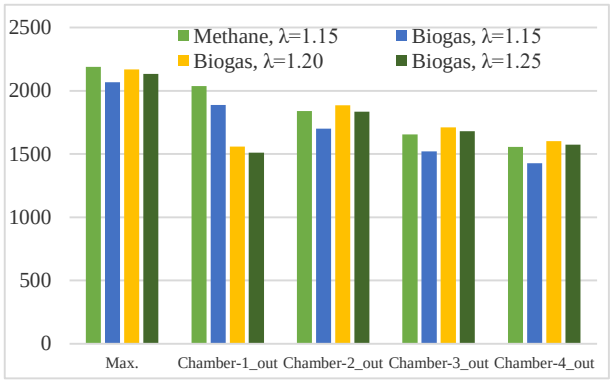

Figure 21. Temperature data for all cases [K].

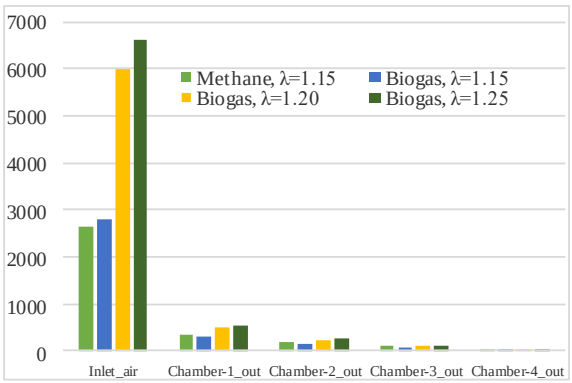

Figure 22. Static pressure data for all cases [Pa].

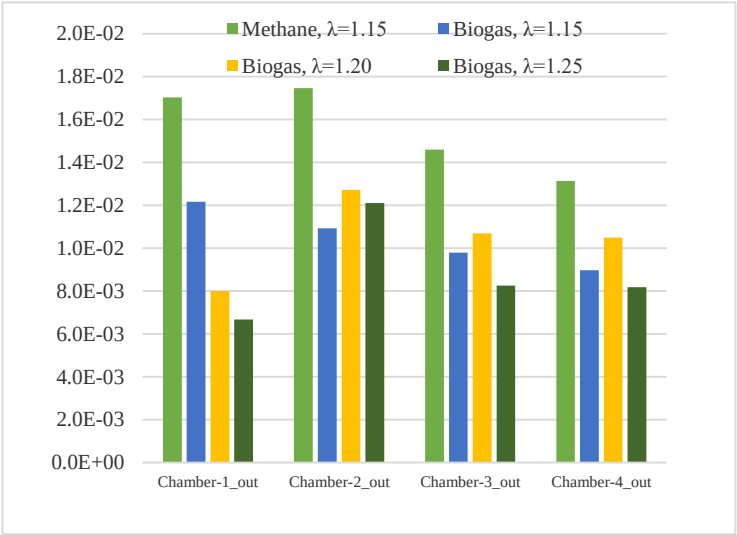

Figure 23. CO mass fraction data for all cases [Pa].

6. Conclusions

A Rankine-type vortex is generated in the first section of the combustor. The flame front is stabilized near the cylindrical wall of the first section, without touching it because the unburnt mixture of fuel and air separates the flame front from the chamber wall. This leads to a reduced thermal load of the cylindrical wall. The two cases with air-excess ratio $\lambda = 1.15$, one with pure methane and the other with biogas, they are quite similar in almost all aspects except the concentration and distribution of

CO. Significantly lower values of CO are generated for biogas combustion, which is mostly due to the presence of a large fraction of CO_2 in the unburnt mixture. The biogas combustion with higher air excess (1.2 and 1.25 respectively) is very different from the combustion of methane or biogas with lower air excess. The most evident difference is the movement of the flame front position from the initial near-wall position at the exterior of the first section to the core vortex boundary. This strongly alters the velocity distribution in all sections and temperature gradient. The solid walls temperature is also significantly changed, with almost the entire surface of the first section external walls barely heated and only one spot at the back of the chamber with higher temperature. The maximum wall temperature is still located in the second section, but the second diaphragm wall is significantly more thermally loaded than the first wall. The CO concentration is higher at $\lambda = 1.2$ than at $\lambda = 1.15$ and the highest concentration is found in the second section of the combustor. The biggest difference is the massively increased pressure loss. This is most certainly the effect of the flame front repositioning, although the actual mechanism of its action is not yet clear.

7. References

[1] Seyed E H, Ghobad B and Mazlan A W 2014 Numerical investigation of biogas flameless combustion, Energy Conversion and Management **81** pp 41–50
[2] Tsuji H, Gupta A K, Hasegawa T, Katsuki M, Kishimoto K and Morita M 2010 High temperature air combustion: from energy conservation to pollution reduction (CRC Press)
[3] Al-Halbouni A, Rahms H and Görner K 2005 *An Efficient Combustion Concept for Low Calorific Gases* Gaswärme-Institut e. V. Essen (GWI) (http://www.icrepq.com/icrepq07/213-al-halbouni.pdf)
[4] Antonescu N N, Stanescu D and Antonescu N 2008 Le bruleur-foyer avec effet Karlowitz pour les gaz de dépots de dechets – essais de performance *Buletinul Stiinţific al Universităţii Politehnica din Timişoara* **53 (67)** Fascicola 1 pp 1-9
[5] Menter F and Egorov Y 2010 The Scale-Adaptive Simulation Method for Unsteady Turbulent Flow Predictions. Part 1: Theory and Model Description *Journal of Flow Turbulence and Combustion* **85** pp 113–138
[6] ANSYS Fluent v.17 Theory Guide 2016 (ANSYS Inc.)
[7] Zimont V 2000 Gas Premixed Combustion at High Turbulence. Turbulent Flame Closure Model Combustion Model *Experimental Thermal and Fluid Science* **21** pp 179–186
[8] Zimont V L and Lipatnikov A N 1995 A Numerical Model of Premixed Turbulent Combustion of Gases Chemical Physics Reports **14(7)** pp 993–1025
[9] Zimont V, Polifke W, Bettelini M and Weisenstein W 1998 An Efficient Computational Model for Premixed Turbulent Combustion at High Reynolds Numbers Based on a Turbulent Flame Speed Closure *Journal of Engineering for Gas Turbines and Power* **120** pp 526–532
[10] Van O A and de Goey L P H 2000 Modelling of Premixed Laminar Flames Using Flamelet-Generated Manifolds *Combustion Science Technology* **161** pp 113–137
[11] Frenklach M et al. 1995 GRI-Mech – An Optimized Detailed Chemical Reaction Mechanism for Methane Combustion (Report No. GRI-95/0058 November 1)

Acknowledgments
The present numerical study was supported by the Computational Fluid Dynamics Laboratory from "Dunarea de Jos" University of Galati, using the ANSYS Fluent v17.1 CFD Solver on the High Performance Computing Cluster (www.hpc.ugal.ro).